



Fabricating high-loading ultra-small PtCu₃/rGO via a traceless protectant and spray-freeze-drying method

Qingyu Luo ¹, Wei Xu ¹, Shaolong Tang ^{*}

National Laboratory of Solid State Microstructure, Collaborative Innovation Centre of Advanced Microstructures, Jiangsu Key Laboratory, Nanjing University, Nanjing 210093, China

ARTICLE INFO

Keywords:

Spray-freeze-drying
Traceless protectant
High-loading
Ultra-small
Oxygen reduction reaction

ABSTRACT

Exploring excellent catalysts for oxygen reduction reaction (ORR) with a facile and cost-effective method is desirable but remains challenging. Herein, ultra-small PtCu₃ nanoparticles (*ca.* 2.7 nm), immobilized on reduced graphene oxide (rGO), were synthesized *via* a novel and general strategy. Traceless protectant, NH₄OH, was used to resist the aggregation of graphene oxide (GO), and the spray-freeze-drying method ensures excellent dispersion of the Pt and Cu precursors, which could not be achieved by other reported drying methods. After annealing, the nanoparticles with the highest mass loading, 52%, among reported ordered Pt-based catalysts were obtained. The PtCu₃/rGO shows a remarkable electrocatalytic performance. Density functional theory calculations elucidate that PtCu₃ possess a lowered energy barrier of the rate-determining step, contributing to significantly improved ORR kinetics. This strategy was extended to the synthesis of other binary- and quaternary-metallic Pt-based nanoparticles, which proved its generality and applicability towards the potential commercialization of fuel cell technologies.

1. Introduction

The rapid consumption of fossil fuels and massive emission of greenhouse gases have urged widespread studies in the exploration of clean energy technologies [1]. Proton-exchange membrane fuel cells (PEMFCs) have attracted significant research attention because of their excellent conversion efficiency with nearly zero-emission [2]. Unfortunately, the oxygen reduction reaction (ORR) at the cathode, involving O₂ absorption, O-O bond cleavage and oxide desorption, performs sluggish kinetics, which is one of the major challenges for the development of PEMFCs [3]. The exceptional electronic structure of Pt endows Pt-based catalysts with superior catalytic activity, providing a solution to sluggish kinetics of PEMFCs at the cathode [4]. However, the high cost and insufficient stability of Pt-based catalysts hamper the practical application of PEMFCs. Hence, intensive efforts have been devoted to investigating high-performance, stable and low-cost electrocatalysts [5–7]. Currently, the mainstream approaches for designing ideal Pt-based catalysts focus on ordered structures composed of Pt and other inexpensive transition metals, which, in contrast to disordered structures, show optimized compressive strain and thereby reduce the dissolution of transition metals and agglomeration of particles during

the catalytic process [8]. It has been reported that a 1% lattice strain could provoke a three-fold enhancement of activity [9]. To lower the proportion of Pt and enhance the catalytic performance, recent advances in this area have been made, including the use of transition metals such as Ti [10], V [11], Cr [12], Mn [13], Fe [14], Co [15], Ni [16], Cu [17], Zn [18], etc.

A general challenge of preparing ordered Pt-M (M = transition metal) nanoparticles (NPs) is the high-temperature annealing process, which is necessary for self-transformation from the disordered phase to the ordered phase but meanwhile leads to inevitable agglomeration of intermetallic NPs. Several strategies have emerged to overcome these problems by the addition of protectants, either on the NPs or the supports, such as oxide coating [14], KCl matrix [19], polymer coating [20], etc. Coating intermetallic particles within a protectant can impede small NPs sintering at high temperatures, serving as a powerful enclosure. For example, Sun et al. demonstrated a MgO-coating method to synthesize 8 nm L1₀-FePt NPs, which shows no aggregation and sintering even after annealing at 700 °C for 6 h [21]. Also, DiSalvo group employed KCl matrix as the protectant in the annealing procedure [19]. In this study, the KCl matrix were removed after calcination to release the ordered Pt₃Ti and Pt₃Cr NPs with a mean size of 6 nm. In addition, to introduce

* Corresponding author.

E-mail address: tangsl@nju.edu.cn (S. Tang).

¹ These authors contributed equally to this work.



the interaction of the support and a protectant can also avoid aggregation of support and downsize NPs [13]. This has been pioneered by the Cui group, taking advantage of the interactions between graphene oxide (GO) and polyvinyl alcohol to prevent GO from aggregation during drying and annealing process, from which synthesized small ordered Pt_3Mn (*ca.* 3 nm) supported on reduced graphene oxide (rGO) [13].

However, the protectants used in the above approaches could be tough impurities in the electrocatalytic system, which lead to potential disadvantages, such as complex experimental processes, undermined the interaction between NPs and supports and low ORR performance. Another drawback is that most of the catalysts required an over 80 wt% support to ensure Pt-M NPs disperse well, resulting in lacking effective electroactive component, *i.e.* the Pt-M NPs, which limits the thinness of catalyst film, increases the mass transfer resistance, and thus weakens electrocatalytic activity [22,23]. Therefore, a novel practical and facile strategy is highly needed to synthesize high-loading ordered Pt-M catalysts with uniform dispersion.

Herein, we report a strategy that uses a traceless protectant and spray-freeze-drying method to prepare high-loading (*ca.* 50 wt%) Pt-M (M = Co, Ni or Cu) NPs uniformly dispersing on rGO. This novel strategy adopted NH_4OH , a reagent easily removed during the drying and annealing process, to reverse the GO aggregation caused by M^{2+} . Besides, a new spray-freeze-drying method was applied to rapidly freeze the solution, minimizing the concentration change and providing homogeneous Pt-M precursor/GO. These advantages synergistically contribute to the high-loading ordered Pt-M NPs with a narrow diameter distribution and ultra-small average size (~ 3 nm). As Cu is more durable than most of the other inexpensive transition metals in electrochemical tests and a good precursor for Pt-based ORR catalysts [24–26], PtCu_3/rGO is used as an example to demonstrate the synthetic mechanism and its electrocatalytic performance. The small size and ordered intermetallic structure furnished O- PtCu_3/rGO with mass activity (MA) 6.5-folds and specific activity (SA) 5.8-folds higher than commercial Pt/C under acidic conditions. Even after 10,000-cycles stability test, O- PtCu_3/rGO catalyst merely shows 3.5% degradation in the MA, while commercial Pt/C performed a 42.4% drop after the stability test. Density functional theory (DFT) calculations also revealed that the intrinsic ORR activity of the ordered $\text{PtCu}_3(111)$ outperforms the Pt(111), which can be contributed to the presence of Cu that decreased the energy barrier of the rate-determining step (RDS) and lowered binding energy of oxygen absorption.

2. Experimental section

2.1. Chemicals

Graphite flakes (100 mesh) were purchased from Ascender Chemical Technology Co., Ltd. (Shanghai, China). Sulfuric acid (H_2SO_4), potassium permanganate (KMnO_4), hydrochloric acid (HCl) and perchloric acid (HClO_4) was purchased from Nanjing Chemical Reagent Co., Ltd. (Nanjing, China). Phosphoric acid (H_3PO_4 , GR) was purchased from Xilong Scientific Co., Ltd. (Shenzhen, China). 30% hydrogen peroxide (H_2O_2) was purchased from Sinopharm Chemical Reagent Co., Ltd. (Beijing, China). Chloroplatinic acid hexahydrate ($\text{H}_2\text{PtCl}_6\cdot6\text{H}_2\text{O}$), copper nitrate hexahydrate ($\text{Cu}(\text{NO}_3)_2\cdot3\text{H}_2\text{O}$), cobalt nitrate hexahydrate ($\text{Co}(\text{NO}_3)_2\cdot6\text{H}_2\text{O}$), nickel nitrate hexahydrate ($\text{Ni}(\text{NO}_3)_2\cdot6\text{H}_2\text{O}$), ammonia solution (NH_4OH), sodium hydroxide (NaOH) and isopropyl alcohol were purchased from Aladdin Reagent Co., Ltd. (Shanghai, China). 20 wt% Commercial Pt/C was purchased from Johnson Matthey Chemicals Ltd. (USA). Nafion was purchased from DuPont Co., Ltd. (USA). All reagents and chemicals were used without further purification.

2.2. Synthesis of GO

GO was synthesized by improved Hummers' method [27]. KMnO_4

(18 g) was dissolved in a mixture of H_3PO_4 (40 mL), H_2SO_4 (360 mL) and graphite flakes (3 g) with stirring. Afterward, the homogeneous suspension was heated to 50 °C and kept for 12 h. After cooling down to room temperature, the dark green solution was slowly poured into *ca.* 400 mL ice. Followed by an injection of excessive 30% H_2O_2 , the color of the reagent changed to golden yellow. After filtered, the remaining mixture was washed with 5% HCl aqueous solution (3×) and deionized water (5×).

2.3. Synthesis of Pt-M/rGO

PtCu_3/rGO catalysts were synthesized by a spray-freeze-drying method followed by an annealing process. In a typical fabrication of PtCu_3/rGO , GO (50 mg C) was dispersed in a mixture of $\text{H}_2\text{PtCl}_6\cdot6\text{H}_2\text{O}$ (67.4 mg, 0.13 mmol), $\text{Cu}(\text{NO}_3)_2\cdot3\text{H}_2\text{O}$ (94.4 mg, 0.39 mmol) and 100 mL deionized water by stirring for 30 min and ultrasonic for 30 min. Then, a 2% NH_4OH aqueous solution was injected to the reaction to make $\text{pH} = 7$, with a $\text{NH}_4\text{OH}/\text{H}_2\text{PtCl}_6$ molar ratio of 8. After ultrasonic for 30 min, the homogeneous suspension was sprayed into liquid nitrogen and then went through a freeze-drying process to obtain a Pt-Cu precursor uniformly dispersed on GO. The intermediate solid was calcined at 350 °C for 20 min to decompose the precursor. Subsequently, the products were calcined under H_2 atmosphere at 600 °C and 700 °C for 2 h to obtain D- $\text{PtCu}_3/\text{rGO}-8\text{NH}_4\text{OH}$ and O- $\text{PtCu}_3/\text{rGO}-8\text{NH}_4\text{OH}$, respectively. To explore the influence of different $\text{NH}_4\text{OH}/\text{H}_2\text{PtCl}_6$ molar ratio on particle sizes, the O- $\text{PtCu}_3/\text{rGO}-x\text{NH}_4\text{OH}$ samples were also prepared according to the similar strategy except setting the $\text{NH}_4\text{OH}/\text{H}_2\text{PtCl}_6$ molar ratios as x ($x = 0, 4, 12, 16$). The O- $\text{PtCu}_3/\text{rGO}-8\text{NaOH}$ were synthesized using a similar strategy as that of O- $\text{PtCu}_3/\text{rGO}-8\text{NH}_4\text{OH}$ except replacing NH_4OH with NaOH.

The PtCo/rGO and PtCoNiCu/rGO were also prepared through the similar procedures except setting the $\text{NH}_4\text{OH}/\text{H}_2\text{PtCl}_6$ molar ratios as 4 and 8, respectively.

2.4. Physicochemical characterization

The crystal phase of the catalysts was identified by an X-ray diffractometer (XRD, Rigaku Ultima IV multipurpose X-ray diffractometer) using a $\text{Cu}-\text{K}\alpha$ radiation source. Thermogravimetric analysis (TGA) of the products was investigated with a simultaneous thermal analysis system (NETZSCH-209F3). The temperature process was started from room temperature to 700 °C in air at a heating rate of 10 °C min^{-1} . Morphological analysis of rGO in the samples was performed with a ZEISS Gemini 500 scanning electron microscopy (SEM). Transmission electron microscopy (TEM) and high-resolution TEM (HRTEM) images were performed with a JM-2100HR JEOL transmission electron microscope operated at the voltage of 200 kV. The high-angle annular dark-field scanning transmission electron microscopy (HAADF-STEM) images and energy dispersive X-ray (EDX) mapping were recorded on a TALOS F200X. X-ray photoelectron spectroscopy (XPS) measurements was carried out on PHI5000 VersaProbe with an $\text{Al}-\text{K}\alpha$ radiation source. The inductively coupled plasma atomic emission spectrum (ICP-AES, Avio 500) was employed to acquire the metal contents of the samples.

2.5. Electrochemical measurements

Electrochemical measurements were conducted on the electrochemical analyzer (CHI 660D). A standard three-electrode system were employed, composed of a glassy-carbon rotating disk electrode (RDE, Pine Research Instrumentation, area: 0.196 cm^2) as the working electrode, a platinum wire as the counter electrode and Ag/AgCl (3 M KCl) as the reference electrode. 4 mg of catalyst were ultrasonically dispersed in a 3:1:0.05 mixture of deionized water/isopropanol/Nafion to prepare a homogenous catalyst ink. 10 μL catalyst ink was transferred onto the working electrode. The loading of Pt on working electrode for all catalysts are 20.6 $\mu\text{g}_{\text{Pt}} \text{cm}^{-2}$ for commercial Pt/C and 18.2 $\mu\text{g}_{\text{Pt}} \text{cm}^{-2}$ for

prepared Pt-M/rGO, which is within the limits of desired loading (7–30 $\mu\text{g}_{\text{Pt}} \text{cm}^{-2}$) [28]. The cyclic voltammetry (CV) was carried out by sweeping the potential between 0.05 and 1.10 V_{RHE} at a scan rate of 50 mV s^{-1} N_2 -saturated 0.1 M HClO_4 electrolyte. Before the electrochemical measurement, 60 cycles of CVs were conducted to electrochemically clean the working electrode. Based on the CV curve, the electrochemical active surface area (ECSA) was determined by the adsorption/desorption regions in the potential range of 0.05–0.40 V_{RHE} and the loading of Pt

$$\text{ECSA}_{\text{Pt,cat}} (\text{m}^2 \text{g}_{\text{Pt}}^{-1}) = \left[\frac{Q_{\text{H-adsorption}} (\text{C})}{210 \mu\text{C} \text{cm}_{\text{Pt}}^{-2} L_{\text{Pt}} (\text{mg}_{\text{Pt}} \text{cm}^{-2}) A_{\text{geo}} (\text{cm}^2)} \right] 10^5 \quad (1)$$

where $A_{\text{geo}} (\text{cm}^2)$ is the geometric surface area of the working electrode (0.196 cm^2). Linear sweep voltammetry (LSV) curves were recorded from 0.2 to 1.1 V_{RHE} with a scan rate of 20 mV s^{-1} in O_2 -saturated 0.1 M HClO_4 electrolyte. To eliminate the capacitive effects during measurement of LSV, background current is subtracted from the ORR current, which was recorded in N_2 -saturated 0.1 M HClO_4 electrolyte. Accelerated durability test (ADT) was carried out by cycling between 0.6 and 1.0 V_{RHE} for 10,000 times at 100 mV s^{-1} in 0.1 M HClO_4 electrolyte. The kinetic density (J_K) can be derived from LSV curve at 1600 r.p.m. using Koutecky-Levich equation.

$$J^{-1} = J_K^{-1} + J_L^{-1} \quad (2)$$

where J is the measured current density (mA cm^{-2}) and J_L is the diffusion limiting current density (mA cm^{-2}). The MA and SA were acquired by normalizing the J_K to the loading Pt mass ($\mu\text{g}_{\text{Pt}} \text{cm}^{-2}$) and real active surface area.

3. Results and discussion

3.1. Synthesis of PtCu_3/rGO

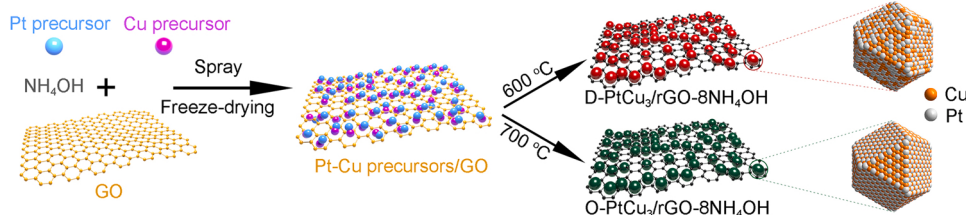
As demonstrated in **Scheme 1**, the facile synthetic strategy involves the addition of the removable NH_4OH aqueous solution, and the use of spray-freeze-drying and the annealing procedures. Firstly, a 2% NH_4OH aqueous solution was injected into the suspension composed of GO and the metal precursors to adjust the reaction pH to *ca.* 7, with a $\text{NH}_4\text{OH}/\text{H}_2\text{PtCl}_6$ molar ratio of 8. Then the reaction underwent a spray-freeze-drying process followed by a high-temperature treatment in H_2 atmosphere. This novel strategy owns two great advantages for fabricating ultra-small PtCu_3 NPs. Firstly, NH_4OH , an agent that can be completely removed through dehydrating and annealing, is employed to reverse the folding of GO in aqueous. Compared with carbon black, GO processes plenty more hydrophilic oxygen groups and a broader surface area. However, the strong interaction between heavy metal ions (Cr^{3+} , Pb^{2+} , Cu^{2+} , etc.) and oxygen groups of GO can easily lead to a reversible aggregation and stacking of GO in an aqueous solution [29]. The injection of NH_4OH aqueous solution transforms Cu^{2+} to $\text{Cu}(\text{OH})_2$, thus decreasing the interaction of Cu^{2+}/GO and regaining the 3D porous structure of GO. As shown in **Fig. S1**, Pt-Cu precursors/GO fabricated in the absence of NH_4OH performs a significant volume-decrease due to the folding and agglomeration of GO, while Pt-Cu precursors/GO synthesized with NH_4OH maintains its fluffy porous structure. SEM analysis is

exploited to further verify the morphologies of Pt-Cu precursors/GO samples dried by different methods (near-infrared light assisted drop-drying method vs. spray-freeze-drying method). The SEM images (**Fig. S2–S3**) confirm the re-dispersion of GO induced by NH_4OH . Secondly, spraying the suspension into liquid nitrogen ensures the uniform dispersion of Pt and Cu precursors on GO. In the traditional freeze-drying method, sufficient time is required for the solution to be completely frozen before drying. Considering the limit of solubility, large and fairly localized ice crystals can be formed under slow cooling rates, which can cause a concentration increase of solutes (20–50 times), further resulting in uneven dispersion of different metal precursors on the supports [30,31]. The spray-freeze-drying method utilized the liquid nitrogen to freeze the aqueous aerosol, which provides the liquid a fast freezing rate to inhibit the crystalline phase and facilitate the glass phase. This method blocks the transport of dissolved species and thus provides homogeneous Pt-Cu precursor/GO [32]. 3D porous structure of GO and homogeneous dispersion of Pt-Cu precursor synergistically contribute to the ultra-small size for PtCu_3 NPs. The catalyst fabricated by annealing homogeneous Pt-Cu precursor/GO at 700 °C for two hours is denoted as O- $\text{PtCu}_3/\text{rGO-8NH}_4\text{OH}$, while the one fabricated by annealing homogeneous Pt-Cu precursor/GO at 600 °C for two hours is denoted as D- $\text{PtCu}_3/\text{rGO-8NH}_4\text{OH}$. For comparison, the catalyst is prepared in the absence of NH_4OH and annealed at 700 °C for two hours is denoted as O- $\text{PtCu}_3/\text{rGO-0NH}_4\text{OH}$.

3.2. Structure characterization

The XRD patterns (**Fig. 1a** and **Fig. S4**) exhibit the intermetallic characteristic of PtCu_3 NPs. As shown in **Fig. 1a**, the diffraction around 24.5° is related to rGO. The two other obvious broad peaks at 42.9 and 49.6°, produced by the ultra-small PtCu_3 NPs, are signed to (111) and (200) planes. Relative to D- $\text{PtCu}_3/\text{rGO-8NH}_4\text{OH}$, the slightly higher-angle shift of O- $\text{PtCu}_3/\text{rGO-8NH}_4\text{OH}$ peaks is due to the lattice contraction, indicating an increased compressive strain and the ordered intermetallic structure. The O- $\text{PtCu}_3/\text{rGO-0NH}_4\text{OH}$ sample, undergoing the same annealing process as O- $\text{PtCu}_3/\text{rGO-8NH}_4\text{OH}$, shows six extra peaks ((100), (110), (210), (211), etc.) in XRD patterns (**Fig. S4**), which indicates its L_{12} ordered structure. The absence of L_{12} ordered phase peak for O- $\text{PtCu}_3/\text{rGO-8NH}_4\text{OH}$ can be owed to the ultra-small average diameter of O- PtCu_3 NPs. As shown in **Table S1**, the ICP-AES result indicates the atomic ratio between Pt and Cu is about 22.4:77.6, which is in good agreement with the molar ratio between Pt and Cu precursors. The loadings of NPs of as-synthesized PtCu_3/rGO catalysts are revealed through TGA (**Fig. 1b**). The corresponding XRD pattern of PtCu_3/rGO after the TGA treatment is shown in **Fig. S5**, which indicates that PtCu_3/rGO is converted to Pt and $\text{Cu}_{0.8}\text{Pt}_{0.2}\text{O}$. According to the proportion of final product in TGA, the proportion of PtCu_3 NPs is determined to be about 52 wt%, which is 2.5-folds of current commercial catalysts (20 wt %).

The XPS is employed to demonstrate the surface chemical state and composition of D- $\text{PtCu}_3/\text{rGO-8NH}_4\text{OH}$ and O- $\text{PtCu}_3/\text{rGO-8NH}_4\text{OH}$ samples. As presented in **Fig. 1c–e**, all XPS spectrums are referred to standard C 1s binding energy (284.8 eV) to eliminate the charge shift. The XPS spectrum for C 1s of D- $\text{PtCu}_3/\text{rGO-8NH}_4\text{OH}$ and O- $\text{PtCu}_3/\text{rGO-8NH}_4\text{OH}$ catalysts (**Fig. 1e**) illustrates three peaks at 284.8, 286.4,



Scheme 1. Schematic demonstrations of fabricating PtCu_3/rGO .

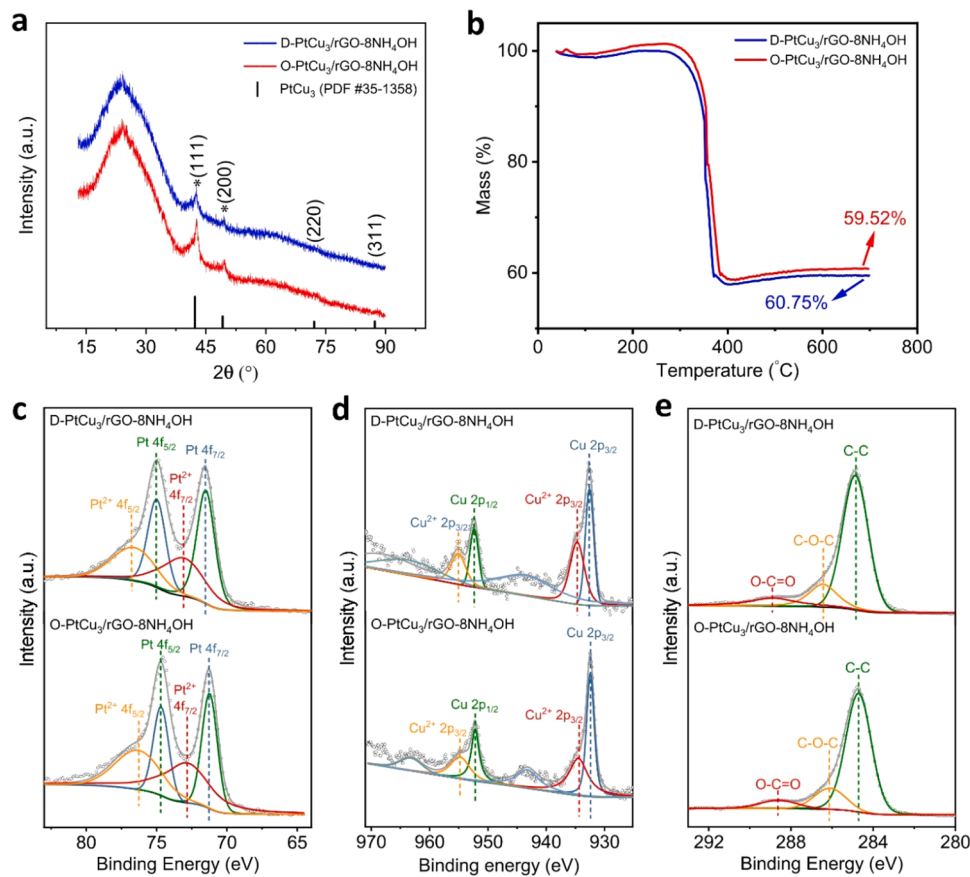


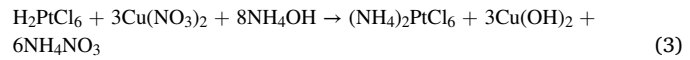
Fig. 1. (a) XRD patterns of D-PtCu₃/rGO-8NH₄OH and O-PtCu₃/rGO-8NH₄OH with the vertical lines referring to the standard diffraction peaks of PtCu₃ (PDF #35-1358). (b) TGA curves of D-PtCu₃/rGO-8NH₄OH and O-PtCu₃/rGO-8NH₄OH. XPS spectra for (c) Pt 4f, (d) Cu 2p and (e) C 1s of the D-PtCu₃/rGO-8NH₄OH and O-PtCu₃/rGO-8NH₄OH samples.

288.9 eV, corresponding to sp^2 C, -C-O and -C=O groups, respectively [33]. The weak intensity of -C-O and -C=O groups confirms the successful reduction of GO to rGO during annealing process. The Pt 4f spectra (Fig. 1c) is fitted with four peaks. For the O-PtCu₃/rGO-8NH₄OH, two peaks located at 71.2 and 74.7 eV are attributed to Pt 4f_{5/2} and Pt 4f_{5/2}, while the near peaks at 72.8 and 76.3 eV are assigned to Pt²⁺. Compared with D-PtCu₃/rGO-8NH₄OH, the O-PtCu₃/rGO-8NH₄OH shows a negative-energy shift (~ 0.4 eV) of Pt 4f, which indicates the decreased d-band center of Pt and reduced 5d electron back-donation from Pt to adsorbates. The latter may contributing to a weakened the interactions of ordered PtCu₃/adsorbates and increased active sites for dissociating O₂, which leads the enhancement of ORR activity [34,35]. The high-resolution Cu 2p spectrum (Fig. 1d) of O-PtCu₃/rGO-8NH₄OH reveals that two main peaks at 932.4 and 952.2 eV are related to Cu 2p_{3/2} and Cu 2p_{1/2}. Moreover, two adjacent low peaks, located at 934.4 and 954.8 eV, are associated with Cu²⁺, which is responsible for the oxidation of surface Cu under air [36]. As displayed in Fig. 1d, the satellite peaks of Cu²⁺ 2p for D-PtCu₃/rGO is more obvious than that of O-PtCu₃/rGO, suggesting that atomically ordered distribution of Pt and Cu could stabilize Cu atom and hinder Cu oxidizing. Furthermore, the XPS spectra results reveal that the surface atomic ratios of Pt/Cu are both 51:49 for D-PtCu₃/rGO-8NH₄OH and O-PtCu₃/rGO-8NH₄OH catalysts, larger than the atomic ratio of Pt/Cu 22.4:77.6 revealed by ICP-AES results. These results indicate Pt atoms segregate on an outer surface of PtCu₃ NPs, which may be induced by annealing under H₂ atmosphere [17].

SEM images indicate the 3D porous architecture (Fig. S6a) and homogeneous dispersion without visible sintering (Fig. S6b) of O-PtCu₃/rGO-8NH₄OH catalyst. The uniform distributions of O-PtCu₃/rGO-8NH₄OH and D-PtCu₃/rGO-8NH₄OH catalysts are further verified by the

TEM images (Fig. 2a-b and Fig. S7). Compared with O-PtCu₃/rGO-8NH₄OH and D-PtCu₃/rGO-8NH₄OH, the O-PtCu₃/rGO-0NH₄OH sample exhibited serious aggregation of PtCu₃ NPs with poor and large size distribution (Fig. S8), which may be resulted from the folding of GO. The insets in the TEM images display a size distribution histogram of corresponding catalysts measured over 200 NPs in random areas. The O-PtCu₃/rGO-8NH₄OH catalyst possesses a much smaller average diameter of about 2.7 nm than that of O-PtCu₃/rGO-0NH₄OH (ca. 10.4 nm), which is consistent with the broaden peaks of O-PtCu₃/rGO-8NH₄OH in XRD pattern. The completely different size distribution of O-PtCu₃/rGO-0NH₄OH and O-PtCu₃/rGO-8NH₄OH catalysts indicates the injection of NH₄OH can effectively prevent GO from aggregation and facilitate mono-immobilization of Pt-Cu precursors on GO.

To further explore the influence of injecting NH₄OH on particle size, the TEM images of the O-PtCu₃/rGO-xNH₄OH synthesized with different molar ratios (x) of NH₄OH/H₂PtCl₆ (x = 0, 4, 8, 12 and 16) are compared and shown in Fig. S9. After injecting the right amount of NH₄OH (x = 8), the reaction in GO aqueous solution is given as follows:



For the O-PtCu₃/rGO-8NH₄OH sample with the right NH₄OH content (Fig. S9c), the PtCu₃ NPs are uniformly supported in rGO with an ultra-small average diameter (~ 2.7 nm). As the amount of NH₄OH is insufficient (x < 8), residual Cu²⁺ in solution causes GO to aggregate and stack, which further leads to aggregation of PtCu₃ NPs (Fig. S9a-b). After adding excess NH₄OH (x > 8), the reaction is transferred as the following equation:

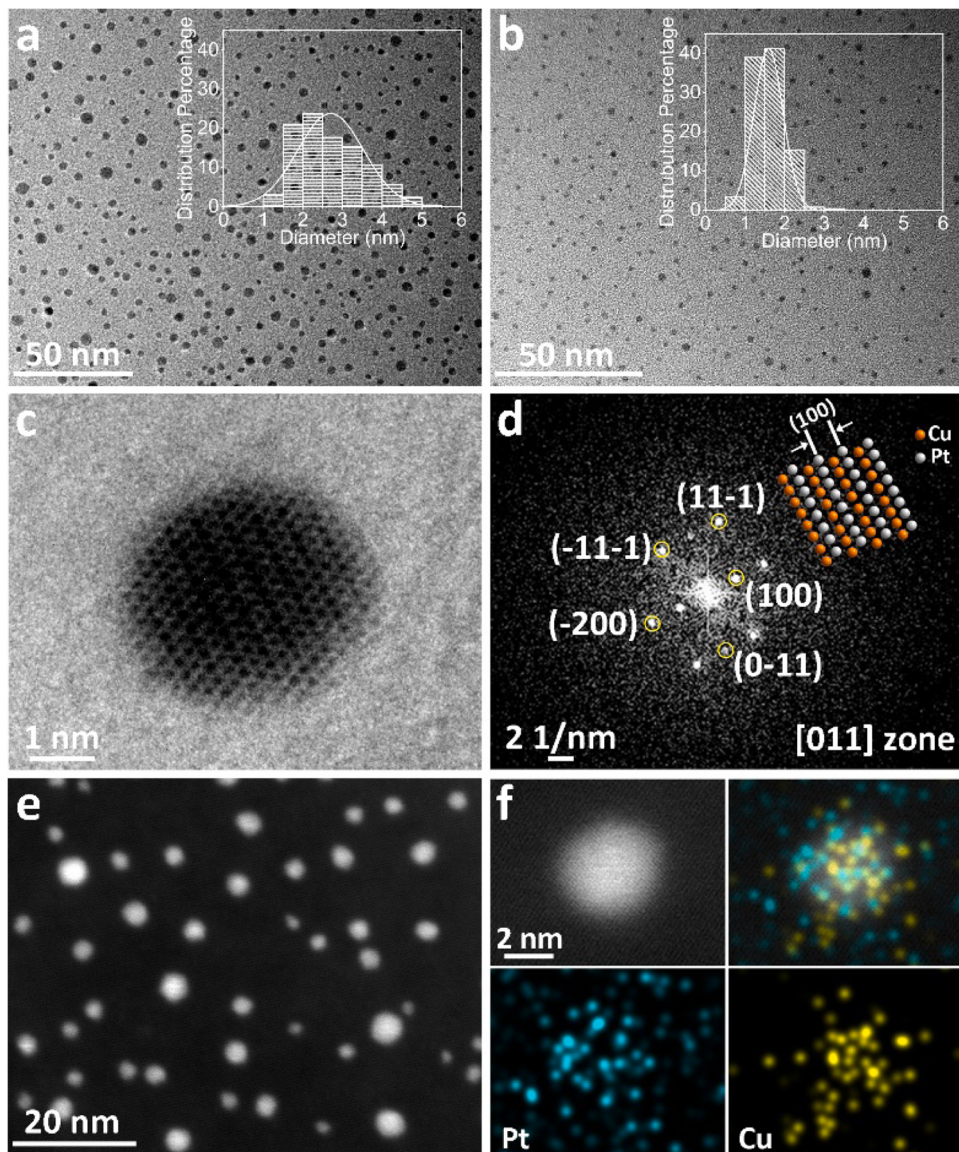
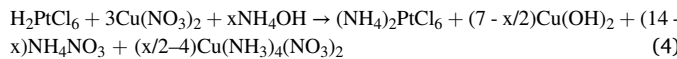


Fig. 2. TEM images of (a) O-PtCu₃/rGO-8NH₄OH and (b) D-PtCu₃/rGO-8NH₄OH, the insets display the corresponding diameter distribution histogram. (c) HRTEM image of O-PtCu₃/rGO-8NH₄OH. (d) FFT pattern derived from panel (c), the inset shows corresponding atomic arrangement along the [011] axis. (e) HAADF-STEM image and (f) EDX elemental mapping image of O-PtCu₃/rGO-8NH₄OH.



In this condition, the concentration of Pt²⁺ shows a sharp drop, which indicates PtCl₆²⁻ and [Cu(NH₃)₄]²⁺ may react to form a precipitate. Not surprisingly, the TEM images (Fig. S9d-e) reveal that the samples prepared with excess NH₄OH show a severe aggregation, where PtCu₃ NPs diameters vary from 3 to larger than 50 nm. Based on these results, we infer that setting NH₄OH/H₂PtCl₆ molar ratio as 8 is optimum for the synthesis of the desired PtCu₃/rGO electrocatalyst. As a comparison, O-PtCu₃/rGO-8NaOH is also synthesized by replacing NH₄OH with NaOH and its TEM image is displayed in Fig. S9f. As a strong base, NaOH transfers Cu²⁺ to a massive precipitate of Cu(OH)₂, making particle size increase to more than 100 nm.

The intermetallic crystallization of O-PtCu₃/rGO-8NH₄OH is revealed by HRTEM. The HRTEM image (Fig. 2c) and corresponding Fast Fourier transforms (FFT) patterns (Fig. 2d) of O-PtCu₃/rGO-8NH₄OH catalyst display superlattice reflections of (100) and (110), verifying the L1₂ ordered structure of PtCu₃ NPs. The diffraction patterns further demonstrate that the absence of distinct characteristic superlattice peaks in XRD results is attributed to the ultra-small size of

O-PtCu₃-8NH₄OH NPs. In contrast, the superlattice reflection is absent for D-PtCu₃/rGO-8NH₄OH (Fig. S10a), indicating its disordered fcc structure. The HAADF-STEM image (Fig. 2e) and EDX element mappings (Fig. 2f) illustrate the homogeneous distribution of Cu and Pt in the O-PtCu₃/rGO-8NH₄OH sample. EDX element mappings also reveal the element ratios between Pt and Cu (23.8:76.2), which is in agreement with ICP-AES results.

3.3. Oxygen reduction catalysis

The electrocatalytic ORR property of O-PtCu₃/rGO-8NH₄OH is investigated and compared with D-PtCu₃/rGO-8NH₄OH and commercial Pt/C (20 wt%) exploiting a rotating disk electrode method. The cyclic voltammetry (CV) profiles obtained in N₂-saturated 0.1 M HClO₄ solution are shown in Fig. 3a. The electrochemical active surface area (ECSA), a significant factor to reflect the active sites, was determined by the absorption/desorption regions in the potential range of 0.05–0.40 V *versus* reversible hydrogen electrode (V_{RHE}) [28]. The O-PtCu₃/rGO-8NH₄OH, D-PtCu₃/rGO-8NH₄OH and commercial Pt/C catalysts

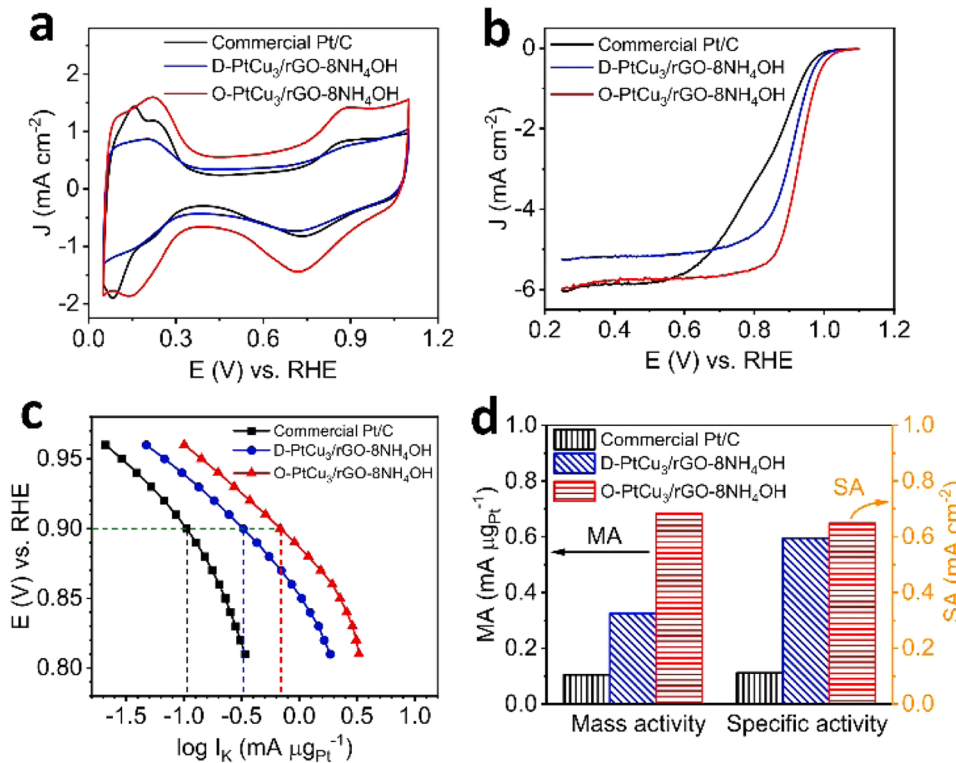


Fig. 3. (a) CV profiles obtained in N₂-saturated 0.1 M HClO₄ solution at a scan rate of 50 mV s⁻¹. (b) ORR polarization curves recorded in O₂-saturated 0.1 M HClO₄ solution (scan rate: 20 mV s⁻¹; rotation rate: 1600 r.p.m.). The background current, measured in N₂-saturated 0.1 M HClO₄ solution, has been subtracted from the results to eliminate the capacitive effects. (c) Tafel plots derived by normalizing kinetic current to Pt loading at different potentials. (d) Mass activities and specific activities of ORR at 0.9 V_{RHE} derived by normalizing kinetic current to Pt loading and ECSA, respectively.

perform ECSA value of 105.4, 54.8 and 93.6 m² g_{Pt}⁻¹, respectively. Obviously, the ECSA value of O-PtCu₃/rGO-8NH₄OH is much larger than D-PtCu₃/rGO-8NH₄OH. The PtCu₃ NPs are transformed from disordered fcc phase to ordered L1₂ phase during high temperature treatment for O-PtCu₃/rGO-8NH₄OH, which may enhance compressive strain, facilitate O₂ diffusion, accelerate electron transport, increase active sites and hence boost the electrocatalytic activity [37].

The positive scanning ORR polarization curves recorded in O₂-saturated 0.1 M HClO₄ solution at a rotation speed of 1600 r.p.m. and a scan rate of 20 mV s⁻¹ are shown in Fig. 3b. The O-PtCu₃/rGO-8NH₄OH displays a higher onset potential value (1.038 V_{RHE}) than that of D-PtCu₃/rGO-8NH₄OH (1.016 V_{RHE}) and Pt/C (1.002 V_{RHE}), suggesting that L1₂ structure stimulates an improved ORR activity. Considering the similar Pt loading for all catalysts, the O-PtCu₃/rGO-8NH₄OH shows an obvious positive shifted half-wave potential (0.924 V_{RHE}) compared with D-PtCu₃/rGO-8NH₄OH (0.904 V_{RHE}) and Pt/C (0.826 V_{RHE}), further demonstrating the superior ORR performance of O-PtCu₃/rGO-8NH₄OH. The MAs and SAs were calculated from ORR polarization curves according to the Koutecky-Levich (K-L) equation by normalizing kinetic current to Pt loading and ECSA, respectively. The kinetic current (mass activities, I_k) at different potential (Tafel plots, Fig. 3c) display the Tafel slopes of all catalysts, an essential indicator to estimate the catalytic efficiency [38]. A low Tafel slope is the key to acquiring large current under low overpotential [39]. Fig. 3c shows that Tafel slope is about 67, 83 and 113 mV dec⁻¹ around 0.9 V_{RHE} for the O-PtCu₃/rGO-8NH₄OH, D-PtCu₃/rGO-8NH₄OH and Pt/C respectively, illustrating the superior efficiency of O-PtCu₃/rGO-8NH₄OH in the ORR catalytic process. Furthermore, Fig. 3c demonstrates the great enhanced kinetic activity of O-PtCu₃/rGO-8NH₄OH compared with that of D-PtCu₃/rGO-8NH₄OH and Pt/C at 0.81–0.96 V_{RHE}. The MA and SA on all catalysts at 0.9 V_{RHE} are both exhibited in Fig. 3d. The O-PtCu₃/rGO-8NH₄OH exhibits MA value of 0.68 mA μg_{Pt}⁻¹, which is much higher than that of D-PtCu₃/rGO-8NH₄OH (0.33 mA μg_{Pt}⁻¹) and Pt/C (0.11 mA μg_{Pt}⁻¹). At 0.9 V_{RHE}, the SAs on O-PtCu₃/rGO-8NH₄OH and D-PtCu₃/rGO-8NH₄OH are 0.65 and 0.59 mA cm⁻², exceeding that of Pt/C (0.11 mA cm⁻²) by 5.7 and 5.3 times, respectively. To further

investigate the electrocatalytic feature of these samples, K-L analysis was employed to carry out catalytic dynamic tests. As illustrated in Fig. S11, the electron-transfer number (n) for all catalysts was evaluated to be about 4, demonstrating that the reduction of oxygen on these catalysts dominantly follows an efficiently four-electron-transfer pathway.

To study the long-term durability of O-PtCu₃/rGO-8NH₄OH, D-PtCu₃/rGO-8NH₄OH and commercial Pt/C catalysts, the ADTs were exploited by scanning the potential in the range of 0.6–1.0 V_{RHE} for 10,000 cycles in O₂-saturated 0.1 M HClO₄ solution. As exhibited in Fig. 4a, the ECSA value of O-PtCu₃/rGO-8NH₄OH and Pt/C gives a decrease of 18.9% and 22.4% after 10,000-cycle ADTs, while the decay in ECSA of D-PtCu₃/rGO-8NH₄OH reaches 50.1%. O-PtCu₃/rGO-8NH₄OH shows improved stability in the CV test, demonstrating that the atomic ordered arrangement of Pt and Cu atoms can decrease the dissolution of Cu atoms and agglomeration of particles during the catalytic process. Generally, the detachment and sintering of NPs, caused by the support degradation and weak NPs/support interaction, are believed to limit the catalytic durability [40]. The TEM images of O-PtCu₃/rGO-8NH₄OH before and after ADTs are further compared to elucidate its excellent durability. The overall morphology of O-PtCu₃/rGO-8NH₄OH (Fig. S12) shows that no evident rGO corrosion appears for high-loading O-PtCu₃/rGO after ADTs. Fig. S11c also illustrates that the average diameter after ADTs only increased by 0.3 nm compared to the initial value (2.7 nm), indicating the excellent durability and dispersion of rGO support and ordered PtCu₃ NPs.

The ORR polarization curves for these catalysts before and after ADTs (Fig. 4b) show that the negligible shift can be observed for O-PtCu₃/rGO-8NH₄OH. Moreover, the half-wave potential of O-PtCu₃/rGO-8NH₄OH performs no detectable shift after ADTs. Contrastingly, serious decay happened to the half-wave potential for D-PtCu₃/rGO-8NH₄OH (~65 mV) and Pt/C (~72 mV) after ADTs. Fig. 4c shows I_k of catalysts before and after ADTs. A slight shift can be observed from I_k for O-PtCu₃/rGO-8NH₄OH at 0.81–0.96 V_{RHE} after 10,000-cycle ADTs, while enormous shifts clearly arose from I_k for D-PtCu₃/rGO-8NH₄OH and Pt/C. The distinct behaviors of catalysts in I_k suggest that O-PtCu₃/

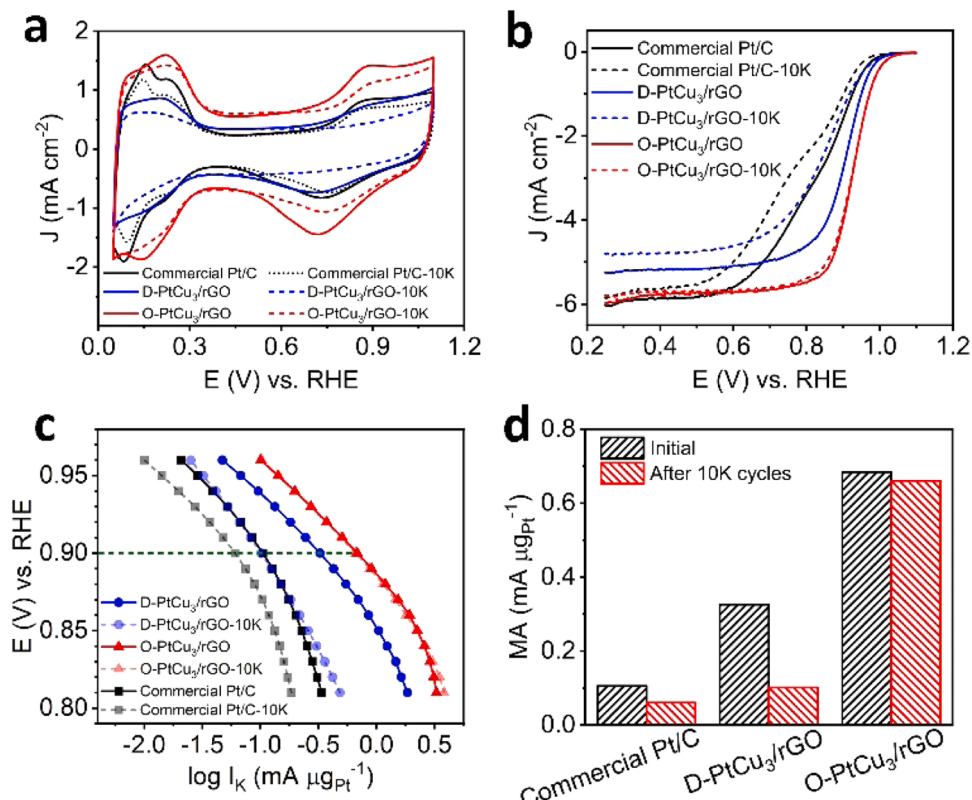


Fig. 4. (a) CV profiles, (b) ORR polarization, (c) Tafel plots and (d) MAs of commercial Pt/C, D-PtCu₃/rGO-8NH₄OH and O-PtCu₃/rGO-8NH₄OH before and after 10,000-cycle ADT.

rGO-8NH₄OH retains most kinetic activity even after 10,000-cycle ADTs and performs the best electrocatalytic stability. For quantitative durability analysis, the MAs of catalysts at 0.9 V_{RHE} before and after ADTs are shown in Fig. 4d. After 10,000 potential cycles, O-PtCu₃/rGO-8NH₄OH still maintain the MA of 0.66 mA $\mu\text{g}_{\text{Pt}}^{-1}$ at 0.9 V_{RHE} with a tiny decay of 3.5%. However, MAs of D-PtCu₃/rGO-8NH₄OH and Pt/C perform a severe drop after ADTs, which are 68.9% and 42.4%, respectively. These results verify the remarkably enhanced catalytic durability of O-PtCu₃/rGO-8NH₄OH catalyst, mainly depending on the strong interactions of metal/support and ordered intermetallic structure of PtCu₃ NPs.

3.4. Catalytic mechanism and theoretical calculations

DFT calculations were performed to study the mechanism in boosting ORR activity of O-PtCu₃/rGO (details in SI). To disclose the role of substrate rGO, we have calculated the combined energy and charge density difference of heterostructures of PtCu₃(111)-p(2 \times 2)/rGO-p(2 \times 2). The combined energy shows a negative value of -2.88 eV, which facilitates the combination of PtCu₃ and rGO. The strong interaction between PtCu₃ and rGO can effectively suppress dissociation and dissolution of PtCu₃ NPs in the electrocatalytic process, which is consistent with the TEM images (Fig. S12) of O-PtCu₃/rGO after 10,000-cycle stability test. As shown in Fig. 5a, the charge density difference illustrates that the effect of substrate rGO on PtCu₃ is mainly concentrated on the interface layer, while the other end of PtCu₃ surface layer is almost unaffected. Based on the above discussion, the influence of substrate rGO is negligible for the following elucidation of the catalytic mechanism.

For comparison, two models, Pt(111)-p(2 \times 2) and PtCu₃(111)-p(2 \times 2), were constructed. Based on our experimental results, the associated mechanism with a four-electrons pathway was adopted for theoretical calculations [41]. The Gibbs free energy diagrams for ORR processes with the two structures, *viz.*, Pt site in Pt(111) and PtCu₃(111)

surfaces were calculated. As shown in Fig. 5b, Pt and PtCu₃ possess a consistent downhill energy pathway at $U = 0$ V_{RHE}, illustrating a spontaneous exothermal process. Upon increasing the potential to equilibrium potential of $U = 1.23$ V_{RHE}, the highest uphill free energy from the third electron transfer step (${}^*{\text{O}} + {\text{H}}^+ + {\text{e}}^- \rightarrow {}^*{\text{OH}}$) determines the RDS for Pt and the energy barrier of RDS is 0.83 eV; while the RDS of PtCu₃ is the first step (${}^*{\text{O}_2} + {\text{H}}^+ + {\text{e}}^- \rightarrow {}^*{\text{OOH}}$) and the energy barrier of RDS is 0.67 eV. Compared to Pt, the lower energy of PtCu₃ indicate a more efficient ORR activity for PtCu₃. Nørskov and co-workers reported that the ORR activity of a catalyst would be better than Pt if its surface binds oxygen 0.00–0.40 eV more weakly than Pt, and the optimum of the volcano plot is around 0.20 eV weaker than that of Pt [42,43]. The calculated oxygen binding energy on PtCu₃ is 0.28 eV weaker than that on Pt (Fig. 5c), demonstrating that Cu atoms may significantly modulate the electronic structure of Pt atoms in PtCu₃.

To further reveal the underlying origin of the superior ORR activity for PtCu₃, charge density differences of oxygen adsorbed intermediate for Pt and PtCu₃ (Fig. 5d) were calculated. The electrons mainly transfer from the active Pt site to O atom. Besides, Bader charge analysis shows that the O adsorbed intermediate gains fewer electrons from PtCu₃ than that from Pt [44], implying that the presence of Cu on Pt can efficiently weaken binding energy of O adsorption. The difference in bonding is usually related to the electronic structures of the surface. Therefore, density of states (DOS) of active Pt site in Pt and PtCu₃ were also presented to investigate the differences in adsorption. As shown in Fig. 5e, the obvious shift of Pt-d orbitals toward lower energy levels can be observed for PtCu₃ compared to Pt. Specifically, the d-band center of the active Pt atom in PtCu₃ is -2.21 eV and that in Pt is -2.05 eV. A more negative value of the d-band center of PtCu₃ would cause an increased antibonding orbitals filling, which decreases the interaction between active Pt site and adsorbates [41]. The introduction of Cu atoms can not only change the ligand environment of Pt atoms, but also bring a variation of the lattice spacing and produce different degrees of strain near

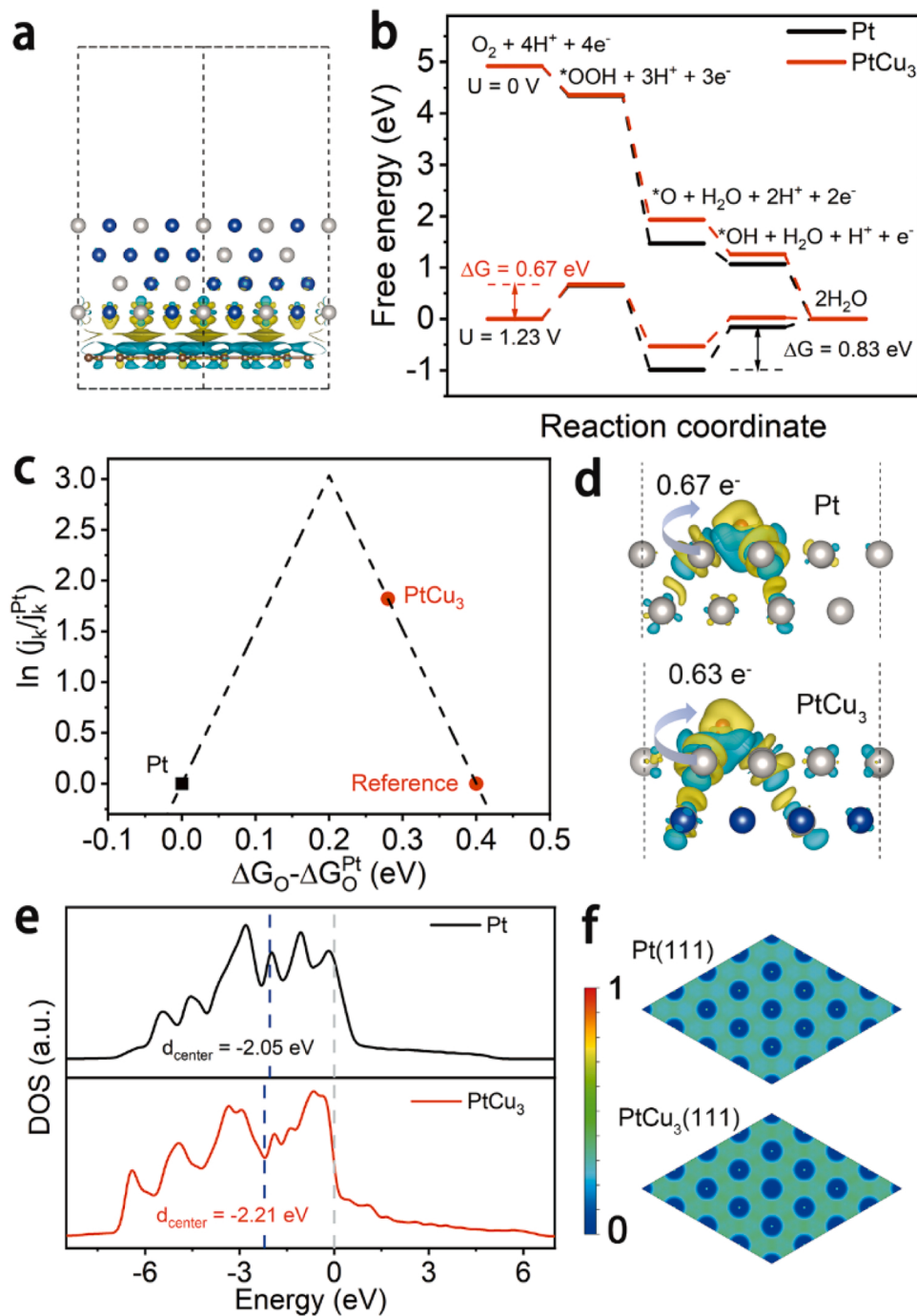


Fig. 5. (a) Charge density difference of PtCu₃/rGO heterostructures. Silver, blue and brown atoms represent Pt, Cu, and C, respectively. The iso-surface value was set to 0.00015 e/Bohr³. Blue represents electron dissipation, and yellow represents electron aggregation. (b) Free energy diagram calculated *via* the DFT method on the associative pathway for Pt (black line) and PtCu₃ (red line) at U = 0 and 1.23 V. (c) Volcano plot including Pt and PtCu₃. j_k is the current density in the experiment and ΔG_0 is the calculated oxygen binding energy. (d) Charge density difference of O adsorbed intermediate for Pt (up) and PtCu₃ (down). Silver, blue and red atoms represent Pt, Cu and O, respectively. The iso-surface value was set to 0.002 e/Bohr³. (e) Density of states of active Pt-d orbitals on Pt and PtCu₃. Fermi level was set to 0. (f) Electron localization function of Pt(111) and PtCu₃(111), respectively. The iso-values of 0 and 1 imply electron delocalized and localized, respectively.

the Pt atoms. These two factors contribute to a modification of electronic structures for Pt atoms. Furthermore, the electron localization function (ELF) analysis (Fig. 5f) shows that the electrons of PtCu₃(111) are more delocalized around the Pt atoms than Pt(111), indicating that PtCu₃ has weaker adsorption, which is consistent with DOS [13,45,46].

3.5. Synthesis of other ordered Pt-M catalysts

To reveal the universality of this strategy, the synthesis process has also been extended to other Pt-M electrocatalytic systems. According to different Pt-M electrocatalytic systems, the molar ratios of H₂PtCl₆/NH₄OH are correspondingly changed (Experimental Section). Using the strategy reported here, binary- and quaternary-metallic electrocatalysts of PtCo/rGO and PtCoNiCu/rGO were synthesized. As shown in Fig. 6a-

b, PtCo/rGO and PtCoNiCu/rGO show narrow size distributions with average sizes of 3.0 and 2.8 nm, respectively. The ordered structures of PtCo/rGO and PtCoNiCu/rGO are verified by their FFT patterns (Fig. 6c-d). The superlattice of (100) indicates the L1₀ ordered structure of PtCo/rGO and the L1₂ ordered structure of PtCoNiCu/rGO. The XRD patterns of PtCo/rGO and PtCoNiCu/rGO are exhibited in Fig. S13. The quaternary-metallic PtCoNiCu/rGO catalyst shows a similar PtM₃ intermetallic diffraction as PtCu₃, while the bimetallic PtCo/rGO catalyst shows the tetragonal structure of PtM. There are no obvious superlattice peaks shown in broadened XRD result (Fig. S13) of PtCo/rGO and PtCoNiCu/rGO, indicating the small size of prepared NPs. Table S2 shows the particle sizes and metallic NP mass loadings of ordered Pt-based catalysts reported in previous works, illustrating that this work successfully avoids the aggregation of high-loading Pt-M NPs.

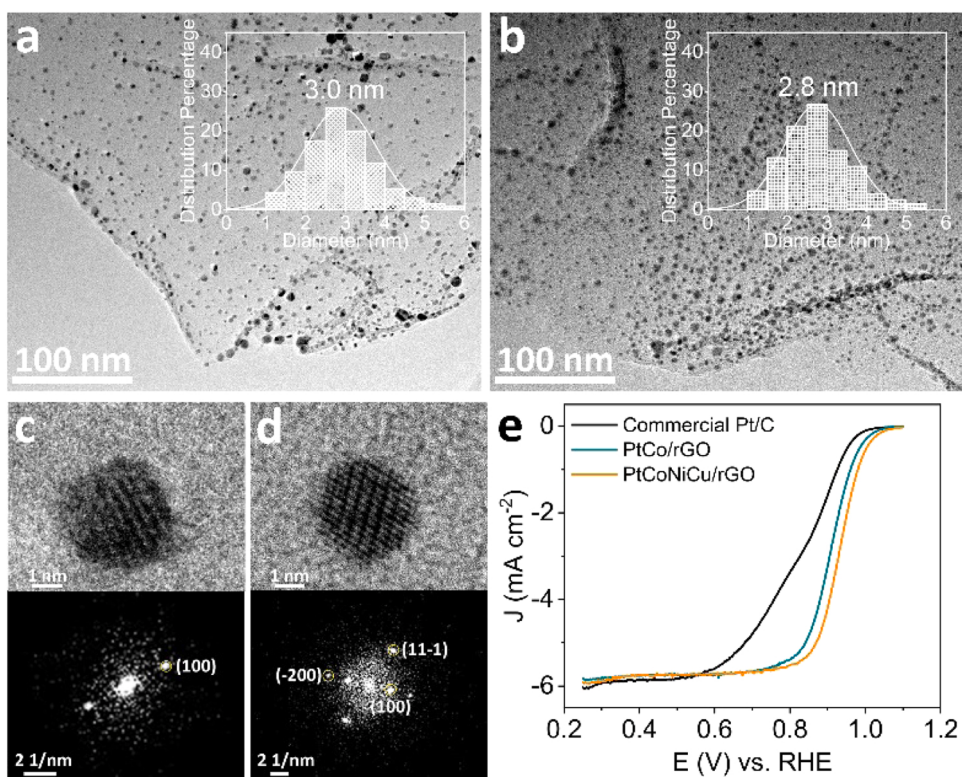


Fig. 6. TEM images of (a) PtCo/rGO and (b) PtCoNiCu/rGO, the insets display the corresponding diameter distribution histogram. HRTEM images and corresponding FFT patterns of (c) PtCo/rGO and (d) PtCoNiCu/rGO. (e) ORR polarizations of commercial Pt/C, PtCo/rGO and PtCoNiCu/rGO.

under high-temperature conditions. The ORR polarization curves of PtCo/rGO and PtCoNiCu/rGO were recorded to estimate their ORR catalytic activity. As shown in Fig. 5e, the half-potentials of PtCo/rGO and PtCoNiCu/rGO show obvious shifts compared with Pt/C (0.826 V_{RHE}), which are 0.907 and 0.930 V_{RHE}, respectively. According to Fig. 6e, the MAs of PtCo/rGO and PtCoNiCu/rGO catalysts are 0.40 and 0.79 mA $\mu\text{g}_{\text{Pt}}^{-1}$, which are 3.6 and 7.2 times higher than that of Pt/C (0.11 mA $\mu\text{g}_{\text{Pt}}^{-1}$). These brief results demonstrate that the strategy is feasible to prepare binary- and quaternary-metallic NPs with different intermetallic structures.

4. Conclusion

We have developed a facial and general method to synthesize intermetallic ordered high-loading PtCu₃ catalysts (53 wt%) with ultra-small average diameter of 2.7 nm. In this strategy, the injection of the transient protectant, NH₄OH, successfully assists GO in resisting folding, and the spray-freeze-drying method ensures the mono-dispersion of Pt and Cu precursors on GO. Promisingly, electrochemical tests indicate significantly improved ORR performance of the prepared catalysts, shown by their activity and stability. At 0.9 V_{RHE}, O-PtCu₃/rGO-8NH₄OH exhibits 6.5 and 5.8 times higher MA and SA than the commercial Pt/C, respectively. Even after 10,000-cycles ADT, O-PtCu₃/rGO-8NH₄OH shows only a negligible drop (3.5%) in MA. DFT calculations unravel the effect of introducing Cu atom to Pt lattice, which can suppress the energy barriers of RDS and boost the ORR activity. We demonstrated that this strategy can be applied to other intermetallic systems. This method opens a new avenue for develop high-loading alloy NPs with enhanced electrocatalytic activity for fuel cells and other clean energy technologies.

CRediT authorship contribution statement

Qingyu Luo: Conceptualization, Methodology, Validation, Formal

analysis, Investigation, Data curation, Writing – original draft, Visualization Preparation. **Wei Xu:** DFT calculation and analysis. **Shaolong Tang:** Resources, Writing – review & editing, Supervision, Project administration, Funding acquisition.

Declaration of Competing Interest

The authors declare that they have no known competing financial interests or personal relationships that could have appeared to influence the work reported in this paper.

Acknowledgements

This work is supported by the National Basic Research Program of China (grant No. 2012CB932304). The numerical calculations in this paper have been done on the computing facilities in the High Performance Computing Center (HPCC) of Nanjing University. The authors also acknowledge Kaiyu Zhang and Lihua Lin for guiding GO support synthesis and thank Yi Liu for her help in editing the manuscript.

Appendix A. Supporting information

Supplementary data associated with this article can be found in the online version at doi:10.1016/j.apcatb.2022.121433.

References

- [1] Y.-J. Wang, H. Fan, A. Ignaszak, L. Zhang, S. Shao, D.P. Wilkinson, J. Zhang, Compositing doped-carbon with metals, non-metals, metal oxides, metal nitrides and other materials to form bifunctional electrocatalysts to enhance metal-air battery oxygen reduction and evolution reactions, *Chem. Eng. J.* 348 (2018) 416–437, <https://doi.org/10.1016/j.cej.2018.04.208>.
- [2] Y. Wang, D.F. Ruiz Diaz, K.S. Chen, Z. Wang, X.C. Adroher, Materials, technological status, and fundamentals of PEM fuel cells - a review, *Mater. Today* 32 (2020) 178–203, <https://doi.org/10.1016/j.mattod.2019.06.005>.

[3] H.A. Hansen, V. Viswanathan, J.K. Nørskov, Unifying kinetic and thermodynamic analysis of 2e⁻ and 4e⁻ reduction of oxygen on metal surfaces, *J. Phys. Chem. C* 118 (2014) 6706–6718, <https://doi.org/10.1021/jp4100608>.

[4] J.K. Nørskov, J. Rossmeisl, A. Logadottir, L. Lindqvist, J.R. Kitchin, T. Bligaard, H. Jónsson, Origin of the overpotential for oxygen reduction at a fuel-cell cathode, *J. Phys. Chem. B* 108 (2004) 17886–17892, <https://doi.org/10.1021/jp047349j>.

[5] X. Wang, X. Zhang, G. Fu, Y. Tang, Recent progress of electrospun porous carbon-based nanofibers for oxygen electrocatalysis, *Mater. Today Energy* 22 (2021), <https://doi.org/10.1016/j.mtener.2021.100850>.

[6] Z. Li, M. Li, X. Wang, G. Fu, Y. Tang, The use of amino-based functional molecules for the controllable synthesis of noble-metal nanocrystals: a minireview, *Nanoscale Adv.* 3 (2021) 1813–1829, <https://doi.org/10.1039/d1na00006c>.

[7] W. Yao, X. Jiang, M. Li, Y. Li, Y. Liu, X. Zhan, G. Fu, Y. Tang, Engineering hollow porous platinum-silver double-shelled nanocages for efficient electro-oxidation of methanol, *Appl. Catal. B: Environ.* 282 (2021), <https://doi.org/10.1016/j.apcatb.2020.119595>.

[8] E. Antolini, Alloy vs. intermetallic compounds: effect of the ordering on the electrocatalytic activity for oxygen reduction and the stability of low temperature fuel cell catalysts, *Appl. Catal. B: Environ.* 217 (2017) 201–213, <https://doi.org/10.1016/j.apcatb.2017.05.081>.

[9] M. Escudero-Escribano, P. Malacrida, M.H. Hansen, U.G. Vej-Hansen, A. Velázquez-Palenzuela, V. Tripkovic, J. Schiøtz, J. Rossmeisl, I.E.L. Stephens, I. Chorkendorff, Tuning the activity of Pt alloy electrocatalysts by means of the lanthanide contraction, *Science* 352 (2016) 73–76, <https://doi.org/10.1126/science.aad8892>.

[10] H. Abe, F. Matsumoto, L.R. Alden, S.C. Warren, H.D. Abruna, F.J. DiSalvo, Electrocatalytic performance of fuel oxidation by Pt₃Ti nanoparticles, *J. Am. Chem. Soc.* 130 (2008) 5452–5458, <https://doi.org/10.1021/ja075061c>.

[11] E. Antolini, R.R. Passos, E.A. Ticianelli, Electrocatalysis of oxygen reduction on a carbon supported platinum–vanadium alloy in polymer electrolyte fuel cells, *Electrochim. Acta* 48 (2002) 263–270, [https://doi.org/10.1016/S0013-4686\(02\)00644-8](https://doi.org/10.1016/S0013-4686(02)00644-8).

[12] Z.M. Cui, H. Chen, W.D. Zhou, M.T. Zhao, F.J. DiSalvo, Structurally ordered Pt₃Cr as oxygen reduction electrocatalyst: ordering control and origin of enhanced stability, *Chem. Mater.* 27 (2015) 7538–7545, <https://doi.org/10.1021/acs.chemmater.5b03912>.

[13] B. Zhang, G. Fu, Y. Li, L. Liang, N.S. Grundish, Y. Tang, J.B. Goodenough, Z. Cui, General strategy for synthesis of ordered Pt₃M intermetallics with ultrasmall particle size, *Angew. Chem. Int. Ed.* 59 (2020) 7857–7863, <https://doi.org/10.1002/anie.201916260>.

[14] Q. Li, L. Wu, G. Wu, D. Su, H. Lv, S. Zhang, W. Zhu, A. Casimir, H. Zhu, A. Mendoza-Garcia, S. Sun, New approach to fully ordered fct-FePt nanoparticles for much enhanced electrocatalysis in acid, *Nano Lett.* 15 (2015) 2468–2473, <https://doi.org/10.1021/acs.nanolett.5b00320>.

[15] D. Wang, H.L. Xin, R. Hovden, H. Wang, Y. Yu, D.A. Muller, F.J. DiSalvo, H. Abruna, Structurally ordered intermetallic platinum–cobalt core–shell nanoparticles with enhanced activity and stability as oxygen reduction electrocatalysts, *Nat. Mater.* 12 (2013) 81–87, <https://doi.org/10.1038/nmat3458>.

[16] L. Chen, J. Zhu, J. Wang, W. Xiao, W. Lei, T. Zhao, T. Huang, Y. Zhu, D. Wang, Phase conversion of Pt₃Ni₂C from disordered alloy to ordered intermetallic with strained lattice for oxygen reduction reaction, *Electrochim. Acta* 283 (2018) 1253–1260, <https://doi.org/10.1016/j.electacta.2018.07.016>.

[17] M. Oezaslan, F. Hasché, P. Strasser, PtCu₃, PtCu and Pt₃Cu alloy nanoparticle electrocatalysts for oxygen reduction reaction in alkaline and acidic media, *J. Electrochim. Soc.* 159 (2012) B444–B454, <https://doi.org/10.1149/2.106204jes>.

[18] Y. Xue, H. Li, X. Ye, S. Yang, Z. Zheng, X. Han, X. Zhang, L. Chen, Z. Xie, Q. Kuang, L. Zheng, N-doped carbon shell encapsulated PtZn intermetallic nanoparticles as highly efficient catalysts for fuel cells, *Nano Res.* 12 (2019) 2490–2497, <https://doi.org/10.1007/s12274-019-2473-x>.

[19] Z. Cui, H. Chen, M. Zhao, D. Marshall, Y. Yu, H. Abruna, F.J. DiSalvo, Synthesis of structurally ordered Pt₃Ti and Pt₃V nanoparticles as methanol oxidation catalysts, *J. Am. Chem. Soc.* 136 (2014) 10206–10209, <https://doi.org/10.1021/ja504573a>.

[20] D.Y. Chung, S.W. Jun, G. Yoon, S.G. Kwon, D.Y. Shin, P. Seo, J.M. Yoo, H. Shin, Y.-H. Chung, H. Kim, B.S. Mun, K.-S. Lee, N.-S. Lee, S.J. Yoo, D.-H. Lim, K. Kang, Y.-E. Sung, T. Hyeon, Highly durable and active PtFe nanocatalyst for electrochemical oxygen reduction reaction, *J. Am. Chem. Soc.* 137 (2015) 15478–15485, <https://doi.org/10.1021/jacs.5b09653>.

[21] J. Li, Z. Xi, Y.-T. Pan, J.S. Spendelow, P.N. Duchesne, D. Su, Q. Li, C. Yu, Z. Yin, B. Shen, Y.S. Kim, P. Zhang, S. Sun, Fe stabilization by intermetallic L₁0-FePt and Pt catalysis enhancement in L₁0-FePt/Pt nanoparticles for efficient oxygen reduction reaction in fuel cells, *J. Am. Chem. Soc.* 140 (2018) 2926–2932, <https://doi.org/10.1021/jacs.7b12829>.

[22] Z. Qi, A. Kaufman, Low Pt loading high performance cathodes for PEM fuel cells, *J. Power Sources* 113 (2003) 37–43, [https://doi.org/10.1016/S0378-7753\(02\)00477-9](https://doi.org/10.1016/S0378-7753(02)00477-9).

[23] Y. Xiong, L. Xiao, Y. Yang, F.J. DiSalvo, H.D. Abruna, High-loading intermetallic Pt₃Co/C core–shell nanoparticles as enhanced activity electrocatalysts toward the oxygen reduction reaction (ORR), *Chem. Mater.* 30 (2018) 1532–1539, <https://doi.org/10.1021/acs.chemmater.7b04201>.

[24] X.-Y. Huang, A.-J. Wang, X.-F. Zhang, L. Zhang, J.-J. Feng, One-step synthesis of PtCu alloyed nanocages with highly open structures as bifunctional electrocatalysts for oxygen reduction and polyhydric alcohol oxidation, *ACS Appl. Energy Mater.* 1 (2018) 5779–5786, <https://doi.org/10.1021/acsaem.8b01385>.

[25] X.L. Chen, G.L. Wen, H. Huang, A.J. Wang, Z.G. Wang, J.J. Feng, Uric acid supported one-pot solvothermal fabrication of rhombic-like Pt₃₅Cu₆₅ hollow nanocages for highly efficient and stable electrocatalysis, *J. Colloid Interface Sci.* 540 (2019) 486–494, <https://doi.org/10.1016/j.jcis.2019.01.020>.

[26] H.J. Niu, H.Y. Chen, G.L. Wen, H.J. Feng, Q.L. Zhang, A.J. Wang, One-pot solvothermal synthesis of three-dimensional hollow PtCu alloyed dodecahedron nanoframes with excellent electrocatalytic performances for hydrogen evolution and oxygen reduction, *J. Colloid Interface Sci.* 539 (2019) 525–532, <https://doi.org/10.1016/j.jcis.2018.12.066>.

[27] D.C. Marcano, D.V. Kosynkin, J.M. Berlin, A. Sinit斯基, Z. Sun, A. Slesarev, L. B. Alemany, W. Lu, J.M. Tour, Improved synthesis of graphene oxide, *ACS Nano* 4 (2010) 4806–4814, <https://doi.org/10.1021/nn1006368>.

[28] Y. Garsany, O.A. Baturina, K.E. Swider-Lyons, S.S. Kocha, Experimental methods for quantifying the activity of platinum electrocatalysts for the oxygen reduction reaction, *Anal. Chem.* 82 (2010) 6321–6328, <https://doi.org/10.1021/ac100306c>.

[29] K. Yang, B. Chen, X. Zhu, B. Xing, Aggregation, adsorption, and morphological transformation of graphene oxide in aqueous solutions containing different metal cations, *Environ. Sci. Technol.* 50 (2016) 11066–11075, <https://doi.org/10.1021/acs.est.6b04235>.

[30] M.C. Heller, J.F. Carpenter, T.W. Randolph, Protein formulation and lyophilization cycle design: prevention of damage due to freeze-concentration induced phase separation, *Biotechnol. Bioeng.* 63 (1999) 166–174, [https://doi.org/10.1002/\(SICI\)1097-0290\(19990420\)63:2<166::AID-BITS>3.0.CO;2-H](https://doi.org/10.1002/(SICI)1097-0290(19990420)63:2<166::AID-BITS>3.0.CO;2-H).

[31] Z. Yu, T.L. Rogers, J. Hu, K.P. Johnston, R.O. Williams, Preparation and characterization of microparticles containing peptide produced by a novel process: spray freezing into liquid, *Eur. J. Pharm. Biopharm.* 54 (2002) 221–228, [https://doi.org/10.1016/S0939-6411\(02\)00050-4](https://doi.org/10.1016/S0939-6411(02)00050-4).

[32] E. Marceau, X. Carrier, M. Che, Impregnation and drying, in: K.Pd Jong (Ed.), *Synthesis of Solid Catalysts*, WILEY-VCH, Weinheim, 2009, pp. 59–82.

[33] J. Cai, W. Liu, Z. Li, One-pot self-assembly of Cu₂O/RGO composite aerogel for aqueous photocatalysis, *Appl. Surf. Sci.* 358 (2015) 146–151, <https://doi.org/10.1016/j.apsusc.2015.08.021>.

[34] J. Cao, Y. Du, M. Dong, Z. Chen, J. Xu, Template-free synthesis of chain-like PtCu nanowires and their superior performance for oxygen reduction and methanol oxidation reaction, *J. Alloy. Compd.* 747 (2018) 124–130, <https://doi.org/10.1016/j.jallcom.2018.03.025>.

[35] W. Li, Z.-Y. Hu, Z. Zhang, P. Wei, J. Zhang, Z. Pu, J. Zhu, D. He, S. Mu, G. Van Tendeloo, Nano-single crystal coalesced PtCu nanospheres as robust bifunctional catalyst for hydrogen evolution and oxygen reduction reactions, *J. Catal.* 375 (2019) 164–170, <https://doi.org/10.1016/j.jcat.2019.05.031>.

[36] Y.-C. Tseng, H.-S. Chen, C.-W. Liu, T.-H. Yeh, K.-W. Wang, The effect of alloying on the oxygen reduction reaction activity of carbon-supported PtCu and PtPd nanorods, *J. Mater. Chem. A* 2 (2014) 4270–4275, <https://doi.org/10.1039/c3ta14705c>.

[37] L.-Y. Jiang, X.-Y. Huang, A.-J. Wang, X.-S. Li, J. Yuan, J.-J. Feng, Facile solvothermal synthesis of Pt₇₆Co₂₄ nanomyriapods for efficient electrocatalysis, *J. Mater. Chem. A* 5 (2017) 10554–10560, [https://doi.org/10.1039/c7ta01976a.](https://doi.org/10.1039/c7ta01976a)

[38] L. Zhang, K. Doyle-Davis, X. Sun, Pt-based electrocatalysts with high atom utilization efficiency: from nanostructures to single atoms, *Energy Environ. Sci.* 12 (2019) 492–517, <https://doi.org/10.1039/c8ee02939c>.

[39] N. Wang, Y. Li, Z. Guo, H. Li, S. Hayase, T. Ma, Minute quantities of hexagonal nanoplates PtFe alloy with facile operating conditions enhanced electrocatalytic activity and durability for oxygen reduction reaction, *J. Alloy. Compd.* 752 (2018) 23–31, <https://doi.org/10.1016/j.jallcom.2018.04.181>.

[40] Z. Song, M.N. Banis, L. Zhang, B. Wang, L. Yang, D. Banham, Y. Zhao, J. Liang, M. Zheng, R. Li, S. Ye, X. Sun, Origin of achieving the enhanced activity and stability of Pt electrocatalysts with strong metal-support interactions via atomic layer deposition, *Nano Energy* 53 (2018) 716–725, <https://doi.org/10.1016/j.nanoen.2018.09.008>.

[41] Z. Wang, X. Jin, C. Zhu, Y. Liu, H. Tan, R. Ku, Y. Zhang, L. Zhou, Z. Liu, S.J. Hwang, H.J. Fan, Atomically dispersed Co₂N₆ and Fe₄N₄ costructures boost oxygen reduction reaction in both alkaline and acidic media, *Adv. Mater.* 33 (2021), 2104718, <https://doi.org/10.1002/adma.202104718>.

[42] J. Greeley, I.E. Stephens, A.S. Bondonaro, T.P. Johansson, H.A. Hansen, T. F. Jaramillo, J. Rossmeisl, I. Chorkendorff, J.K. Nørskov, Alloys of platinum and early transition metals as oxygen reduction electrocatalysts, *Nat. Chem.* 1 (2009) 552–556, <https://doi.org/10.1038/nchem.367>.

[43] V. Stamenovic, B.S. Mun, K.J.J. Mayrhofer, P.N. Ross, N.M. Markovic, J. Rossmeisl, J. Greeley, J.K. Nørskov, Changing the activity of electrocatalysts for oxygen reduction by tuning the surface electronic structure, *Angew. Chem.* 118 (2006) 2963–2967, <https://doi.org/10.1002/ange.200504386>.

[44] G. Henkelman, A. Arnaldsson, H. Jónsson, A fast and robust algorithm for Bader decomposition of charge density, *Comput. Mater. Sci.* 36 (2006) 354–360, <https://doi.org/10.1016/j.commatsci.2005.04.010>.

[45] A.D. Becke, K.E. Edgecombe, A simple measure of electron localization in atomic and molecular systems, *J. Chem. Phys.* 92 (1990) 5397–5403, <https://doi.org/10.1063/1.458517>.

[46] A. Savin, O. Jepsen, J. Flad, O.K. Andersen, H. Preuss, H.G. von Schnering, Electron localization in solid-state structures of the elements: the diamond structure, *Angew. Chem. Int. Ed.* 31 (1992) 187–188, <https://doi.org/10.1002/anie.199201871>.